Oxygen vacancy modulated MnO_2 bi-electrode system for attomole-level pathogen nucleic acid sequence detection

Highlights:

- Fabricated an inexpensive bi-electrode electrochemical sensor for nucleic acid amplification detection with a user-friendly interface in a short detection time.
- Electronic conduction of the metal oxide sensing layer was successfully optimised by manipulating the concentration of oxygen vacancies.
- The sensing layer was annealed at various temperatures and optimised by testing their electrical, optical, and chemical properties.
- The fabricated device was able to detect dengue virus sequence DNA and Staphylococcus aureus genomic DNA with clinically relevant limit of detection.

Oxygen vacancy modulated MnO_2 bi-electrode system for attomole-level pathogen nucleic acid sequence detection

Tanvi Agarkar [a,#], Vandana Kuttappan Nair [b,#], Sayantan Tripathy [b], Vipin Chawla [c], Souradyuti Ghosh [b]; Ashvani Kumar [a,*]

[a]Department of Physics, Bennett University, India

[b]Department of Chemistry, Bennett University, India

[c]Institute Instrumentation Centre, Indian Institute of Technology Roorkee, India

[#]Joint first authors

*Corresponding author: ashuiit19@gmail.com

Abstract:

DNA amplification detection is typically a lengthy and sophisticated procedure involving high-end instrumentation. Electrochemical detection has recently opened a relatively low budget, a straightforward and speedy method for detection with the aid of an electrochemically active redox probe. However, electrochemical sensors of nucleic acid amplification characteristically employ a tri-electrode geometry involving standard reference electrode usually made up of a noble metal that adds up the cost of detection. This work proposes a sensitive and rapid approach for detecting the endpoint of nucleic acid amplification test using a novel bi-electrode sensing geometry. The sensing layer of the electrode was comprised of a transition metal oxide to tune its electronic state for regulating its electrochemical response. The fabricated device was then used to detect dengue virus sequence DNA (using rolling circle amplification) and *Staphylococcus aureus* genomic DNA (using polymerase chain reaction) with the limit of detection in the order of 10^3 target DNA copies.

Keywords*: DNA amplification; Electrochemical biosensor; Methylene blue; Oxygen vacancy; Metal oxide*

1. Introduction:

Nucleic acid amplification tests (NAATs) are routine biological processes with applications in pathogen detection, identifying food and water contamination, diagnosing genetic diseases, and biowarfare prevention. It is an essential step in the biomedical analysis as the amount of DNA found in numerous biological samples is at a concentration low enough that direct detection is not possible.[1] It, therefore, necessitates the intervention of NAATs to make millions to billions of copies of the target nucleic acid followed by quantitative detection. Several methods are practised for nucleic acid amplification amongst which polymerase chain reaction (PCR) has remained the most preferred technique. However, it involves a sophisticated sequence of thermal steps and precise temperature control.[2],[3] These requirements of PCR have spurred the advancement of various isothermal amplification techniques such as loop-mediated isothermal amplification (LAMP), recombinase polymerase amplification (RPA), and rolling circle amplification (RCA).[4]

Currently, the quantification of NAATs is usually done using a fluorescent DNA binding dye or sequence-specific probe technique.[5–7] The dye (e.g. SYBR green) binds to the minor grooves of double-stranded DNA only and emits fluorescence in the bound state with an intensity of > 1000 folds compared to its unbound states.[8] The intensity of the fluorescence is proportional to the amplified product.[5] In the probe-based technique, an amplicon sequence-complementary nucleic acid probe carrying a reporter molecule (at the 3’ end) and a quencher dye (at the 5’ end) is utilized. In real-time PCR, Taq DNA polymerase then cleaves the nucleic acid probe to generate fluorescence to quantify the amount of DNA amplified using NAAT.[9] Alternatively, a molecular beacon with complementarity to the amplicon sequence and carrying a fluorescence/quencher

pair could also be utilized.[10,11] Such fluorometric methods, though accurate and used as a standard practice, are laborious, lengthy, and expensive. They also require trained hands for operations and real-time. An attractive alternative to optical detection has been proposed based on the electrochemistry of the DNA-binding redox probes.[12] Advantageously, electrochemical techniques are sensitive to electrochemically responsive species (redox probes) irrespective of background light and sample colour as in the case of fluorometric methods.[13–15] At the same time, such measurements could be carried out in electrochemical workstations that are significantly inexpensive compared to real-time PCR instruments.

An electrochemical biosensor is a transducer of oxidation (or reduction) of an electroactive species to an electrical current signal. The electrochemical activity of DNA is not adequate for direct detection, therefore a redox indicator is employed for the purpose.[16] The device senses the redox probe concentration and the variation in mass transfer to the working electrode. Since DNA has a strong affinity for redox probe, the binding significantly reduces the “free” probe concentration in the electrolyte. After DNA amplification high concentration of amplicons (i.e., replicated DNA) are produced that captures a greater number of probe molecules which in turn reduces the electrochemical signal.[16–18] Commonly used redox probes are transition metal complexes (e.g. ruthenium (Ru) complexes[19–21]) and organic dyes (e.g. methylene blue (MB), a thiazine class probe with the molecular formula $C_{16}H_{18}N_3SCl$ [17,18,22],[23]). Jiong Zhang[21] et al. employed ruthenium hexamine for the amplified detection of BRCA-1 mutant DNA, whereas Naoki Nagatani[17] et al. and Kuangwen Hsieh[18] et al. used MB for electrochemical monitoring of influenza virus RNA and quantitative detection of pathogenic DNA, respectively. In the present

work, MB is employed as a redox probe as shown in SI Figure 1. It binds to the DNA electrostatically as well as intercalates into the DNA structure.[24]

The electrochemical biosensors of nucleic acid and NAAT detection reported to date commonly uses 3-electrode assembly with platinum (Pt) and/or silver/silver chloride (Ag/AgCl) as standard reference and counter electrode, and gold (Au) or commercially available screen-printed carbon electrode as a working electrode.[18,22],[25],[26] Despite their inexpensive nature and possibility of electronic state modulation, the utility of the transition metal oxides in sensing nucleic acids and NAATs has remained surprisingly underexplored. This work aims to present an inexpensive and novel modus operandi for amplified detection of DNA with a user-friendly interface in a short detection time. We have fabricated an electrochemical bi-electrode sensing device (EBSD) consisting of a thin layer of transition metal oxide (TMO) deposited on FTO coated glass as a working electrode and silver wire as a quasi-reference counter electrode (QRCE) (Figure 1a). Several manganese oxides such as MnO, MnO_2, and Mn_2O_3 are popularly used as electrode materials in electrochemical sensing .[27–29] MnO_2 is one of the most common manganese oxides with a wide range of applications in molecular adsorption, energy storage, biosensing, and memory devices.[29–34] It has excellent biocompatible properties which makes it a popular candidate in biosensing. We hypothesized that creating oxygen vacancies in the MnO_2 sensing layer will improve its conduction state and thus enhances the sensitivity of our device towards detecting any minute change in the concentration of DNA binding redox probe. Hence, sol-gel spin-coated MnO_2 is used as the sensing electrode and its electronic conduction states are manipulated by annealing at various temperatures. To prevent rapid evaporation of electrolyte and ensure uniform contact area among various electrodes, a PDMS micro-cavity is integrated

onto them. For testing, 5μl of sample amount is loaded in the PDMS cavity that in turn cut down the cost of reagents. The device was then utilized in detecting dengue virus (DENV) serotype-2 sequence (using rolling circle amplification or RCA) and vancomycin resistance-associated regulator gene (*vraR*) gene in *Staphylococcus aureus* (*S. aureus*) genomic DNA (using PCR) and tested on the EBSD. The EBSD results are then compared with standard fluorescence readout employing RT-PCR instrument.

2. Experimental details:

2.1. Materials:

All chemicals were analytical reagent (AR) grade and used without further purification. Manganese acetate Mn $(CH_3COO)_2 \cdot 4H_2O$, ethoxyethanol ($C_4H_{10}O_2$), spermidine, dithiothreitol (DTT), methylene blue (MB), and monoethanolamine (MEA) (C_2H_7NO) were purchased from SRL chemicals. Polyethylene glycol (PEG) ($C_{2n}H_{4n+2}O_{n+1}$) was purchased from CDH chemicals. Fluorine-doped tin oxide (FTO) deposited glass, and 99.99% pure silver wire were purchased from commercial sources and cleaned with isopropyl alcohol (IPA) before use. Silicone Elastomer Kit comprised of Base/Curing Agent was purchased from SYLGARD 184 to formulate Polydimethylsiloxane (PDMS) layer. Oligonucleotides were purchased from either Eurofin or Sigma with “desalting” purity and then used without any further purifications. The phi29 enzyme, T4 polynucleotide kinase (PNK) enzyme, T4 DNA ligase enzyme, adenosine triphosphate (ATP), dNTP, BSA and Phi29 buffer were procured from New England Biolab, USA. SYBR™ Green I Nucleic Acid Gel Stain 10,000X was purchased from Invitrogen. PCR mix (with and without SYBR Green I)

was purchased from HiMedia, India. Ultrapure water dispensed from a Millipore Milli-Q Type I water purification system, which was then double autoclaved was utilized in preparing all solutions and dilutions. Phosphorylation, annealing, and ligation reactions were performed in an Eppendorf Mastercycler Nexus system. Real-time RCA studies were carried out in Bio-Rad CFX96 qRT-PCR and analysed using CFX Maestro software.

2.2. Method:

2.2.1. Preparation of MnO_2 thin film:

MnO_2 sensing layer was coated onto FTO substrate using the sol-gel spin coating method. The solution was prepared by dissolving $Mn(CH_3COO)_2 \cdot 4H_2O$ metal salt in a mixture of ethoxyethanol solvent, MEA and PEG, where MEA acts as a stabiliser and PEG is used as a binder.[35] A 0.5 M of precursor solution was prepared and stirred at room temperature (RT) for 30 min on a magnetic stirrer. When the salt is completely dissolved, it is filtered using a 0.22-micron pore size syringe filter and kept aside for ageing for at least 12 hrs at room temperature. The obtained solution was spin-coated onto FTO coated glass substrate.

FTO substrate was partially covered with a physical mask to prevent the deposition of the sensing layer onto the substrate to make electrical contact. The rotation speed and deposition time were optimised to achieve uniform deposition, the schematic presentation of the deposition method is shown in SI Figure 2. The deposited films were dried at $\sim 170^\circ$ for 10 min on a hot plate followed by the annealing at the temperatures of $350, 450, \text{and } 550°C$, respectively. MnO_2 deposited FTO electrodes annealed at $350, 450$, and $550°C$ are referred to as FM350, FM450, and FM550, respectively.

2.2.2. Preparation of PDMS layer:

PDMS patches were fabricated by mixing the base and curing agent in a ratio of 10:1, respectively in a glass petri dish. The dish was desiccated for 5 min to burst any air bubbles inside the mixture and baked for 30 minutes at $70°C$. After ambient cooling, the resulting 2 mm thick PDMS was cut in a rectangular piece of 2×2.5 cm^2 dimensions and individual cavities of 0.25 cm diameter were made using a hole punch plier.

2.2.3. *Assembling the device:*

The PDMS patch and the as-prepared electrode was cleaned using IPA, the patch was adhered onto the sample by activating the PDMS using a UV ozone activator. The holes were filled with 5μL of the desired electrolyte using a micropipette. A silver (Ag) QRCE was immersed in the micro-cavity to complete the bi-electrode geometry. The real-time assembled EBSD sensor is shown in SI Figure 3.

2.2.4. Preparation of methylene blue solutions

The methylene blue solutions were prepared in 10 mM Tris-HCl buffer pH 7.5. The buffer itself was made in non-DEPC treated ultrapure Milli-Q type I water (double-autoclaved). It was noted that DEPC treated water led to unwanted redox peaks in I-V experiments. The dilutions of methylene blue (e.g., 100, 50, 25, 12.5 μM) were carried out using serial dilution using the same buffer as diluent.

2.2.5. *Electrode characterisation:*

The structural, electrical, compositional, and optical properties of the fabricated films are probed by various characterisation tools. The optical band gap was obtained using an Ocean Optics UV-vis spectrophotometer within the wavelength range of 200-900 nm. The oxidation state of as-synthesized MnO_2 was examined by X-ray photoelectron spectroscopy (XPS) (Physical Electronics, PHI 5000 VersaProbe III) in the energy range of 0-1200 eV using the Al monochromatic X-ray source. The sample surface morphology was studied by Field-Emission Based Scanning Electron Microscope (FESEM) (FEI Quanta 200 F) at 20kV. Electrochemical impedance spectroscopy (EIS) measurements were performed using Metrohm Autolab Potentiostat/Galvanostat (Model Autolab PGSTAT302N). All the current-voltage measurements were recorded using Keysight B2912A source measurement unit (SMU).

2.2.6. *Preparation of circular DNA*

2.2.6.1. *5′-Phosphorylation:*

Precursor ssDNA oligonucleotide 5’-GTC GCT TTT AGA GTA GAT GAG TGC AAG CCT TTA GCG ACG TCC AGT CCG CGA ACC ACA TCA TCC CTA AGT CCA CTA CAC CAT GCG TAC CTC AGC TTT GGA CTG GAC-3’ was diluted to 8 μM. The oligonucleotide was designed so that it would fold itself to a dumbbell shape, thus bringing it's 5’- and 3’-termini adjacent to each other and allowing a self-annealing ligation. The oligonucleotide solution was snap-cooled (5 minutes heating at 95°C immediately followed by 5 minutes incubation on ice) to linearize the DNA for improving the phosphorylation efficiency. The 5’-phosphorylation was carried on the oligonucleotides (final concentration 4 μM) in presence of T4 PNK (0.375 Units μL^{-1}), ATP (1 mM), ligase buffer (50 mM

Tris-HCl pH 7.5, 10 mM $MgCl_2$, 1 mM ATP, 10 mM DTT), DTT (5 μM), and spermidine (1.7 mM). The addition of all the reagents was performed on ice. The solution was incubated at 37°C for 3 hours followed by annealing by slow (1 h) cooling from 95°C to 4°C (this step also inactivated the T4 PNK).

2.2.6.2. Ligation:

Circularization of the annealed 5′-phosphorylated DNA (concentration 3.2 μM for self-annealing precursor, 1.6 μM for sticky-end precursors and 3.2 μM for the padlock) was carried out in presence of T4 DNA ligase (8 Cohesive End Units μL^{-1}), ATP (1 mM), and T4 DNA ligase buffer (50 mM Tris-HCl pH 7.5, 10 mM $MgCl_2$, 1 mM ATP, 10 mM DTT). The addition of all the reagents was done on ice. The ligation mixture was then incubated at 16°C for 16 hours followed by enzyme inactivation at 75°C for 20 min. The ligation efficiency was checked in 13% denaturing PAGE gel. The actual concentration of the circularized oligonucleotide was calculated using the unligated linear oligonucleotide loaded in the same gel as the reference.

2.2.6.3. Exonuclease treatment:

The ligated sample was snap-cooled as described in the phosphorylation section. The exonuclease digestion was carried out in 25 μL reaction volume as described below. Both exonuclease I (2.4 units μL^{-1}) and III (12 units μL^{-1}) were added in 1X exonuclease III buffer (10 mM Bis-Tris-Propane-HCl pH 7, 10 mM $MgCl_2$, 1 mM DTT). The reagents were added while keeping the centrifuge tubes on ice. The solutions were incubated at 37°C for 4 hours, followed by enzyme inactivation at 85°C for 20 minutes and then stepwise annealing from 85°C to 4°C to generate the desired secondary structure.

2.2.7.Real-time (fluorescence) and electrochemical rolling-circle amplification (RCA) of DNA:

The RCA reactions were carried out in presence of primer (5'-TAC GCA TGG TGT AGT GGA CT-3', a sequence from DENV serotype-2) and hyperbranched RCA (HRCA) primer (5'-GCG AAC CAC ATC ATC-3'). For linear RCA or LRCA reactions, the oligonucleotide substrates (circular DNA and primer) were first incubated at 30°C for 30 min in 50 mM Tris-HCl (pH 8) and 50 mM NaCl. For hyperbranched RCA or HRCA reactions, an additional HRCA primer was also added to the above mix. The real-time-RCA reactions was carried out in 25 μL volume in presence of circular DNA (0.02 μM), primer (concentration 2 fM – 0.02 nM), HRCA primer (0.2 μM, present only for HRCA reactions), dNTPs (1.0 mM), BSA (0.2 μg uL^{-1}), phi29 buffer (50 mM Tris-HCl pH 7.5, 10 mM $MgCl_2$, 10 mM $(NH_4)_2SO_4$, 4 mM DTT), 0.4X SYBR Green I, and phi29 DNA polymerase (0.2 units μL^{-1}). All the reagents except circular DNA, primer, HRCA primer, Tris-HCl (50 mM, pH 8.5), and NaCl (50 mM) were added as a mastermix. The reactions were incubated for 2 h at 30°C and fluorescence intensities were recorded in 2 min intervals. For the electrochemical RCA, the SYBR was replaced with MB (100 μM), and the experiment was incubated for 2 hrs at $30°C$ followed by inactivation at $70°C$ for 20 min in an Eppendorf Mastercycler^R nexus system. For measurement of electrochemical endpoint, the completed reaction was transferred to ice and immediately subjected to measurement on the EBSD. In these experiments, NTC refers to no-target control, where the LRCA or HRCA reaction was carried out only in presence of circular DNA alone (as well as HRCA primer for HRCA conditions) but in the absence of primer. TC refers to target control, where both circular DNA and primer (as well as HRCA primer for HRCA conditions) was present.

2.2.8.Genomic DNA isolation from S. aureus:

1 mL of an overnight *S. aureus* (N315) culture in tryptic soya broth (HiMedia) was taken into a 1.5 mL microcentrifuge tube and centrifuged for 2 minutes at 5000 × g to pellet the bacteria. The pellet was re-suspended in 500 µL of lysostaphin solution (200 µg/mL lysostaphin; 20 mM Tris-HCl, pH 7.5; 10 mM EDTA). After incubating at 37°C for at least thirty minutes, proteinase K (HiMedia) was added to a final concentration of 100 µg/mL and incubate at 56°C for an hour. Phenol:chloroform:isoamyl alcohol (SRL) was added to the culture at a ratio of 1:1 followed by centrifugation at max speed (~12,000 - 13,000 × g) for 10 minutes. The aqueous top layer was transferred to a new microcentrifuge tube and NaCl was added to a final concentration of 200 mM. 100% isopropanol (Merck) was added to the culture at a ratio of 1:1 and incubated at -20^{0}C for 30 minutes and centrifuged at maximum speed (~12,000 - 13,000 × g) for 10 minutes followed by removal of supernatant carefully. 1 mL of ice-cold 70% ethanol was added and again centrifuged at maximum speed (~12,000 - 13,000 × g) for 10 minutes and the supernatant was discarded. After air drying, the transparent pellet was re-suspended in 100 µL TE buffer.

2.2.9.Real-time and electrochemical PCR amplification

In each case, the assay was performed in 25 µl solution. The stated concentration of genomic DNA was added to 1X real-time PCR mix containing Taq DNA polymerase, 0.4 mM dNTP, SYBR Green I (or 50 µM MB for electrochemical PCR), and 1X Taq buffer (10 mM Tris-HCl, 50 mM KCl, 1.5 mM $MgCl_2$, (pH 8.3 at 25°C)), 0.4 µM forward and reverse primer against *vraR* gene (sequences 5'-CCATGAGTTGAAGCCAGATTT-3' and 5'-CCTGCATCTAATGCACGATA-3', respectively) and molecular grade water. All reagents except the template DNA (*S. aureus* genomic DNA) was added as a mastermix. PCR was set at the following settings: 95°C for 180 seconds, then 39 cycles of 95°C for

10 seconds, 52°C for 10 seconds, and 72°C for 30 seconds. For real-time PCR, this was followed by melt curve analysis. For measurement of electrochemical endpoint, the completed reaction was transferred to ice and immediately subjected to measurement on the EBSD.

3. Result and Discussion:

3.1. Design and concept:

The working principle of the proposed device relied on the dynamic electrochemistry at the interface of the sensing material and the electrolyte. The device was composed of three components: a working electrode, an ionic conductor (electrolyte), and a quasi-reference counter silver electrode (QRCE) as shown in Figure 1a. The working electrode was comprised of a conducting substrate (FTO), employed as a current collector, coated with metal-oxide semiconductor (MnO_2) film act as a sensing layer. The EBSD picked up electrochemical signal by recording the current-voltage (I-V) characteristics under the sweeping voltage of -1 to +1 V and back. We hypothesized that the optimal modulation of the electronic conduction states of the sensing layer would result in the sensitive detection of any electrical change at the electrode-electrolyte interface (e-e interface). This in turn would help detect the ionic current arising out of concentration variation of the DNA-binding redox dye. Oxygen vacancies ($V_o^{\cdot\cdot}$) were thus introduced into the metal-oxide sensing layer to manipulate their conducting states via annealing at various temperatures (Figure 1b).[36]

During the formation of $V_o^{\cdot\cdot}$, lattice oxygen (O_o^x) was converted to oxygen gas (O_2) and led to the generation of free electrons (e') as per the equation given below[37]:

$$O_o^x \leftrightarrow V_o^{\cdot\cdot} + 2e' + \frac{1}{2}O_2(g)$$

These additional electrons would thus magnify the electronic conductivity of the sensing layer. These newly generated electrons caused disorder in the lattice and produced new localised energy levels near the conduction band minima.[38,39] The extended conduction band was directly reflected in the optical absorption onset in the Tauc plot for the MnO_2 electrodes (SI Figure 4). It demonstrated a reduction in optical band gap (SI Figure 4 (inset)) with increased annealing temperature to the lowest value of 3.33 eV[40],[41] for FM550. The observed results were in consonance with the results reported for ZnO, TiO_2, and SnO_2.[38,39,42,43]

The proposed device measured the change in total current density (J_t) which is the sum of the contribution from ionic (J_i) and electronic ($+J_e$) current densities. The electron transfer took place through the localised states to the ions in the electrolyte at the e-e interface. The rate of electron transfer was higher than their rate of diffusion in the bulk of the ionic liquid as a result an electric field was established in the bulk electrolyte. Consequently, the ions drifted to neutralize the field and to negate the corresponding variation of their electrochemical potential (Figure 1c). Ultimately, the electrolyte would carry out the ionic conduction, and the localised states at the e-e interface would be responsible for the electronic conduction. The current density for ionic and electronic charge carriers is described (in 1-D) by the following equations,[44]

$$J_i = qn_i\mu_i E - qD_i\frac{\partial n_i}{\partial x}$$

$$J_e = qn_e\mu_e E + qD_e\frac{\partial n_e}{\partial x}$$

Where, q, n, μ, E, and D are the electric charge, the number of charge carriers, carrier mobility, applied electric field and diffusion coefficient, respectively.

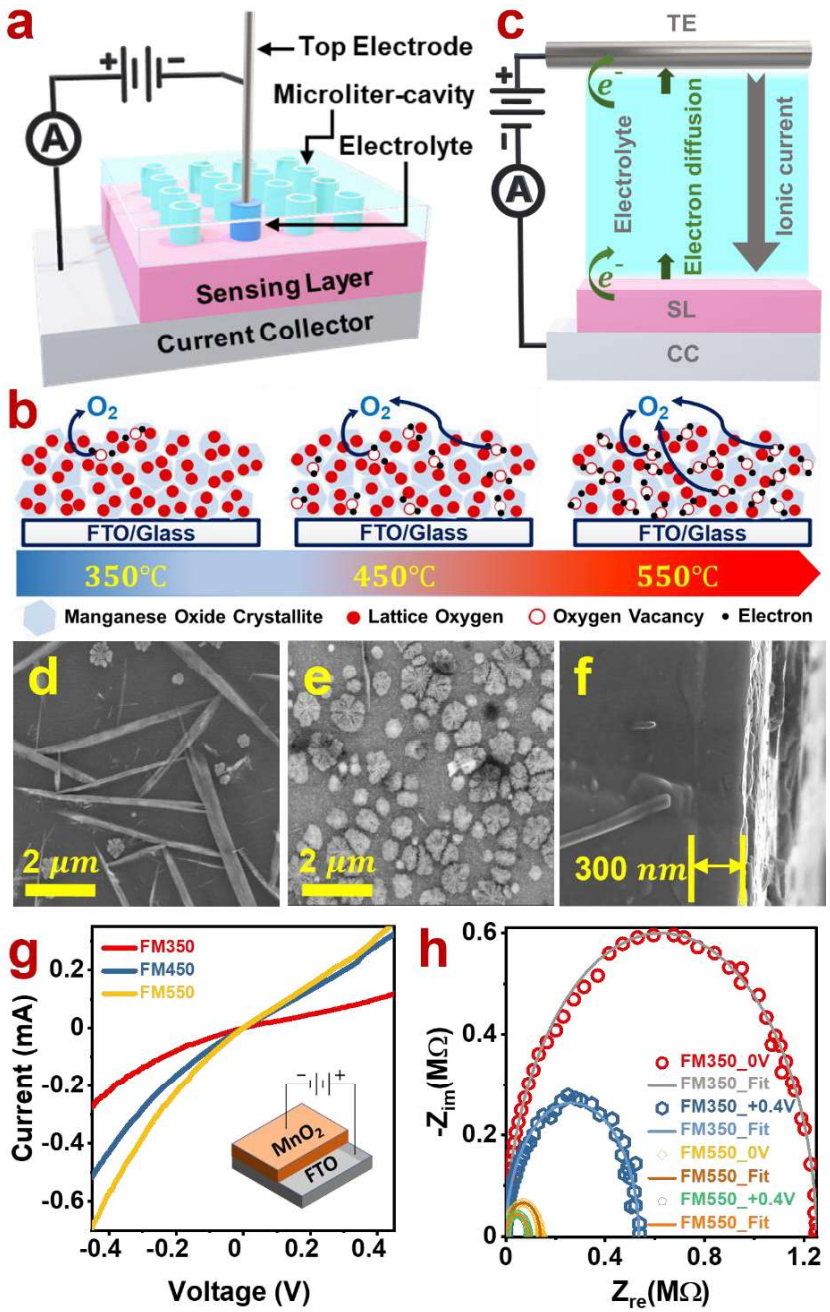

Figure 1 Electrode geometry, concept, and characterization including morphology and electrical measurements. (a) Electrochemical Bi-electrode sensing device (EBSD) schematic. (b) Schematic showing increase in oxygen vacancies with temperature. (c) Charge transport kinetics (TE-top electrode, IL-ionic liquid, SL-sensing layer, CC-current collector). (d-f) SEM images of FM350-FM550

surface and FM550 cross-section displaying the film thickness, respectively. (g) DC conductivity of FM350-FM550 device (inset shows electrical connections for the measurement). (h) AC conductivity for FM350 and FM550 at 0 V and 0.4 V.

3.2. Characterisation of as-fabricated sensing electrode:

3.2.1. Morphological study and Film-substrate junction electrical analysis:

The surface morphology of the electrodes was studied using FESEM, while the current-voltage (I-V) characteristic was recorded to study the electrical behaviour of the film and substrate interface. Figure 1d and 1e show the surface morphology of FM450, and FM550 electrodes and Figure 1f depicts a cross-sectional image of FM550 film revealing the film thickness to be 300 nm, respectively. For FM450 film strewn micro-rods structure with an approximate average length of 5 μm along with distributed micro-flower structures were observed. On the other hand, a structural transformation from micro-rod to micro-flowers was observed for FM550. This could be due to the crystalline phase transition of MnO_2 to Mn_2O_3 or the co-existence of more than one phase of manganese oxide. In the case of FM550, micro-flowers of ~0.5 μm diameter was found to be uniformly distributed across the surface.

The current-voltage (I-V) characteristics of FTO/MnO_2 junction is performed for FM350, FM450, and FM550 electrodes between -0.9 to +0.9 V using 100 μM MB and found to be demonstrating weak rectifying behaviour (Figure 1g) similar behaviour was reported for WO_3 film deposited on FTO coated glass.[45] The current is limited by the contact resistance comprising of the series resistance of metal oxide film and junction resistance. The contact resistance calculated for a linear region above + 0.25V for FM350, FM450, and FM550 is presented in SI Table 1 with FM550 having the lowest contact resistance. Thus, the electrical property of the electrodes improved

with increasing annealing temperature due to the presence of higher oxygen vacancy concentration which was independently confirmed using XPS results discussed later in the manuscript. Next, the AC conductivity of FM350, and FM550 was measured using electrochemical impedance spectroscopy at DC voltages of 0 and +0.4 V over a frequency range of 1Hz to 1MHz, respectively. The corresponding Nyquist plots ($-Z_{im}$ vs. Z_{re}) (Figure 1h) were fitted with an equivalent electric circuit (EEC) having resistance in series (R_s) to a parallel combination of film resistance (R_f) and constant phase element (Q_f) as shown in SI Figure 5. The n-value of all the four plots is very close to "1" indicating the capacitive nature of Q_f (SI Table 2). A sharp decline in the R_f and rise of C_f value with increased annealing temperature indicated receding solid-state interface layer resistance of FTO/MnO_2 that have originated due to higher concentration of oxygen vacancies.

3.2.2. XPS analysis of MnO_2 sensing layer:

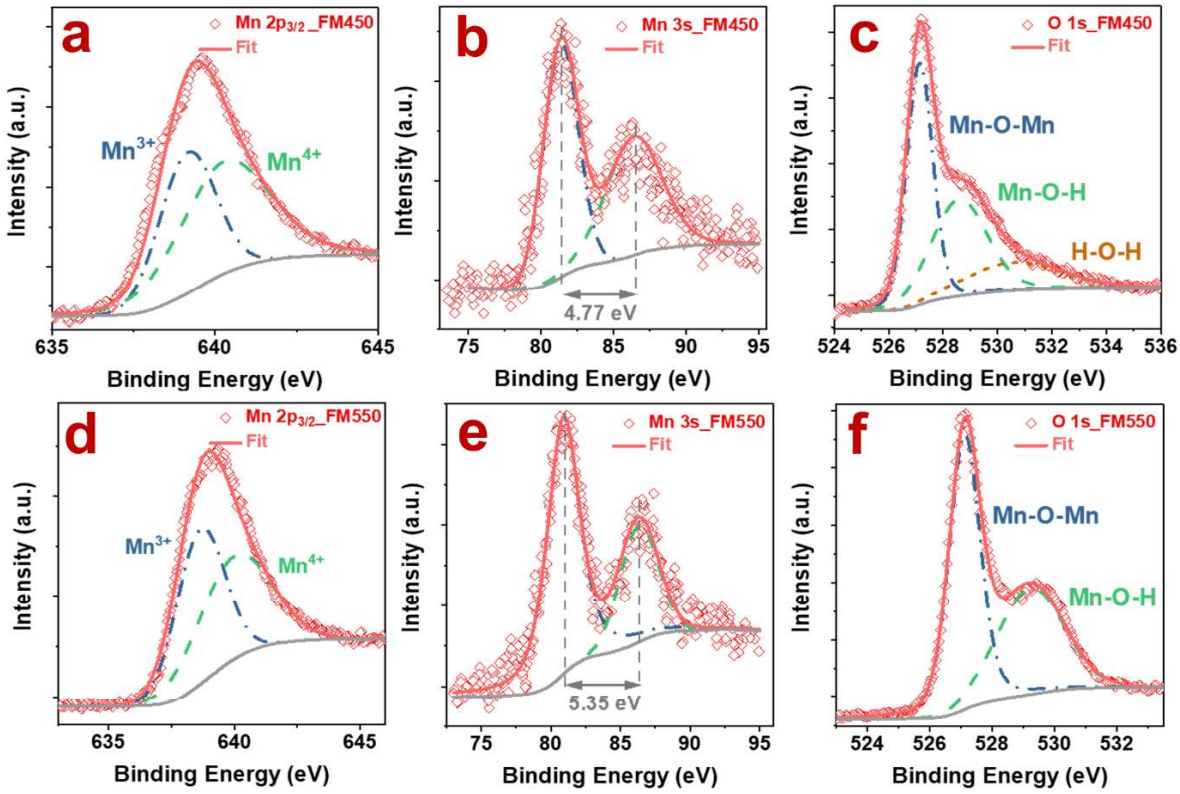

Figure 2 XPS spectra for (a, d) Mn $2p_{3/2}$; (b, e) Mn 3s; (c, f) O 1s of FM450 and FM550, respectively.

The oxidation state of Mn was evaluated using highly-surface-specific XPS technique for FM450 and FM550 films. The XPS pattern results were fitted with Gaussian-Lorentzian peak (G-L peak) and are presented in Figure 2 following subtraction of the Shirley background. The peak of Mn $2p_{3/2}$ (Figure 2a, d) was deconvoluted into two G-L peaks at the binding energy (B.E.) values of 638.8 and 640.8 eV, corresponding to Mn^{3+} and Mn^{4+} for FM450 and at 639.2 and 640.45 eV for FM550, respectively.[34,46] The peak separation denoted by ΔE_s in Mn 3s spectra (Figure 2b, e) for FM450 is 4.77 eV[47,48] whereas it is 5.35 eV for FM550 revealing the dominance of MnO_2 over Mn_2O_3 in FM450 then in FM550. The surface average oxidation state (AOS) of Mn was calculated using the formula: $AOS = 8.956 - 1.126\ \Delta E_s$.[49,50] The AOS value reduced

significantly from 3.58 to 2.94 suggesting the creation of more oxygen vacancies on the sample surface due to the heat treatment of the sample at elevated temperature.

The O1s (Figure 2c and 2f) core-level spectra is deconvoluted into P1, P2, and P3 peaks at 527.15, 528.65, and 530.75 eV for FM450 and P1', and P2' peaks at 527.12 and 529.26 eV for FM550. The P1 (P1') peaks attributed to Mn-O-Mn, P2 (P2') and P3 peak corresponds to Mn-O-H and H-O-H, respectively. By comparing the relative area of P2 (37.57) and P2' (43.18) peaks for the two films, a greater hydroxide (OH^-) concentration was observed in FM550. The superior OH^- content results in a highly active surface area that ensures efficient conduction across the interface.[51] Thus, the XPS results conclusively assures improved conduction and sensing response of FM550.

3.3. Electrode optimisation:

3.3.1. Electrochemical impedance measurement:

To understand the conduction mechanism of sensing electrodes, all three devices in the presence of 100 µM-MB electrolyte are tested under the oscillating potential of 10 mV at DC voltage of -0.45 V over the frequency range of 1 MHz to 1 Hz (Figure 3a). The EIS data were analysed by fitting an EEC to the FTO-MnO_2-electrolyte system (Figure 3b). The familiar Randles circuit was modified by introducing an additional time constant and used as an EEC. Here R_s represents the ohmic solution resistance of the electrolyte, the electric double-layer capacitance is substituted by a constant phase element (Q_{dl}) $(Z_{CPE} = 1/Y_0(j\omega)^n)$ considering film inhomogeneity, R_{ct} is the charge transfer resistance, and W $(Z_w = /\omega^{1/2} - j\sigma/\omega^{1/2}; \sigma = 1/\sqrt{2} \cdot Y_0$ at $\omega = 1\ rad/s)$ is the Warburg resistance that models the linear ionic charge diffusion towards the electrode. The additional time constant is used to model the FTO-MnO_2 interface since charge carriers primarily

travel through the film before interacting with the substrate. It consists of a parallel combination of a capacitor (C_f) and a resistance (R_f).[52,53] All the values of equivalent circuit elements are compiled in Table 1. The average value of R_s for all the devices is obtained to be $\sim 500\ \Omega$. The carrier lifetime (τ) for any interface represented by an RC-circuit can be calculated from the well-known relation, $\tau = R * C$, where R and C are the resistance and capacitance value in the circuit (Table 1). A decrease in τ value from FM350 to FM550 is correlated with increased conductivity. The *n*-value of the Q_{dl} for FM350 is 0.68 that portrays capacitive nature of the electrode, whereas FM550 is more resistive in nature with an *n*-value of 0.59.

The FM550 device has a higher slope in the linear section of the Nyquist plot and shorter projection on the real axis as compared to other devices, this suggests lower Warburg resistance and thus faster ion diffusion at the e-e interface**.**[54]

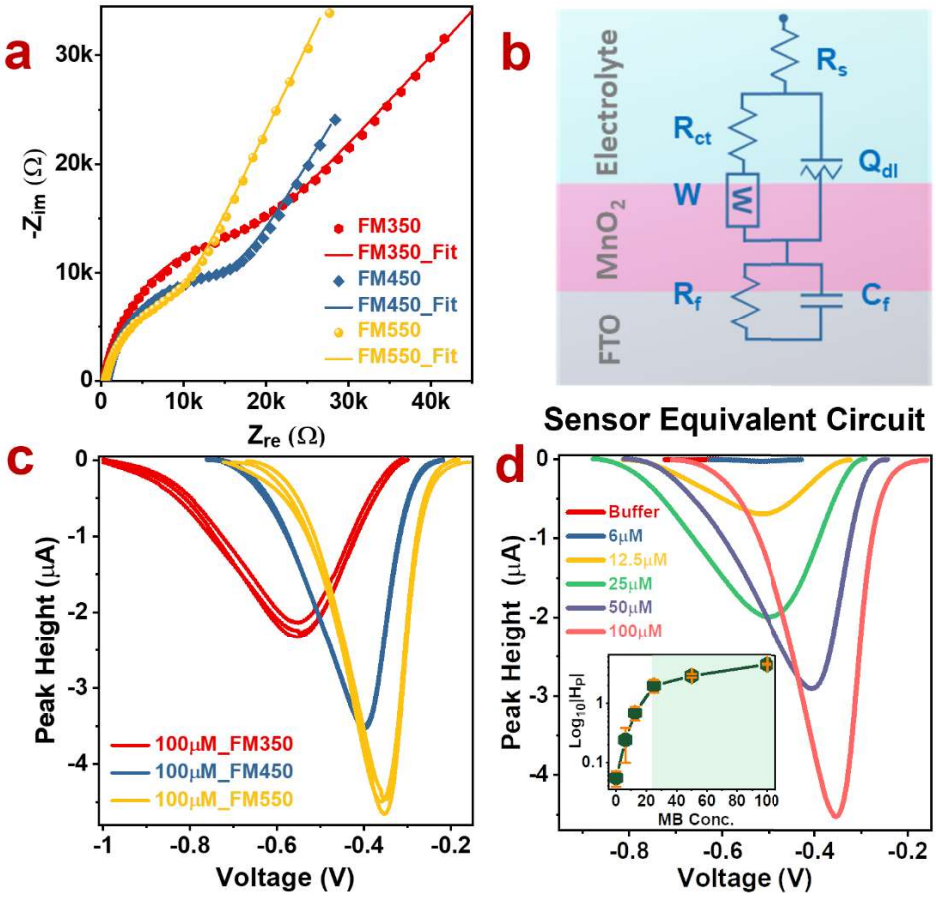

Figure 3 Electroanalytical results comparing the performance of FM350, FM450, and FM550 electrodes using EIS and I-V characteristics. (a) EIS Nyquist plots of FM350, FM450, and FM550 devices with 100 μM concentration of MB in Tris-HCl buffer (10 mM, pH 7.5). (b) Electrode-electrolyte interface with equivalent electrical circuit used to fit impedance spectra for Nyquist plots (c) and I-V characteristics (baseline corrected) comparing the performance of FM350, FM450, and FM550 devices for 100 μM-MB concentrations. (d) and I-V characteristics (baseline corrected) showing the impact of various MB concentrations on the performance of FM550 [Inset: MB concentration vs. Log_{10}(peak height) with error bar for n=7 cycles].

Table 1 Summary of parameters obtained by fitting EIS Nyquist plot

Element	**Parameter**	**FM350**	**FM450**	**FM550**
Solution resistance ($R_s \backslash \Omega$)	R	346.54	504.37	482.9
Film resistance ($R_f \backslash k\Omega$)	R	11.50	9.7	5.4
Film capacitance ($C_f \backslash \mu F$)	C	0.7	0.75	0.88
Time constant ($\tau \backslash$ ms)	R_f * C_f	8.05	7.03	4.95
Charge-transfer resistance ($R_{ct} \backslash k\Omega$)	R	66	5.7	2.53
Double-layer constant phase element (Q_{dl})	Y_0 ($\mu S * s^n$)	3.5	0.105	6.68
	n	0.68	0.665	0.595
Warburg impedance (W)	Y_0 ($\mu S * s^{1/2}$)	6.50	1.28	1.19

3.3.2. Current-voltage measurements:

I-V characteristics of the EBSD with sensing electrodes FM350, FM450, and FM550 were compared to optimise the working electrode. The external applied voltage was swept from an initial voltage (-1 V) to a final voltage (+1 V) and back for multiple cycles and the average value is presented. The baseline correction was applied by subtracting a straight line connecting the two extremes of the reduction peak. The peak height (H_P) values for FM350, FM450, and FM550 are -2.68 μA, -3.51 μA and -4.52 μA, respectively. The I-V measurements for each electrode have been repeated 3-times and are represented in Figure 3c. Superior electrocatalytic activity of FM550 device was observed plausibly due to large surface area of micro-flower structure and enhanced electron-transfer ability due to the higher accessible area, and therefore shorter charge diffusion path.[55],[54] Increased electrical conductivity of FM550 results in shifting of reduction peak voltage (-0.35 V) towards more anodic potential compared to FM450 (-0.4 V) and FM350 (-0.54 V)

electrodes which suggest easier electron transfer across the interface. After the superiority of the FM550 electrode has been established, it is therefore utilized for further studies in this work.

3.4. Validation of Redox Probe and NAAT Detection with Electrochemical Readout:

To understand electrochemical behaviour, the FM550 device was tested under varied concentrations of MB ranging as 100, 50, 25, 12.5, and 6 μM, respectively (Figure 3d). The reduction peak intensity was found to be decreasing with lower MB concentration due to the reduced amount of electron transfer at the e-e interface resulted from lower ionic conductivity of MB. The concentration versus peak height (H_p) was plotted in the inset of Figure 3d, suggested a linear range from 25-100 μM that was used further for device application. The I-V measurements were also performed at different scan rates on FM550 using 100 μM MB solution (SI figure 6a). It shows a quasi-reversible behaviour of the reaction with current directly proportional to scan rate suggesting a current response for surface absorbed analyte (SI section- 6).

Also, to establish the importance of MnO_2 in the device geometry and on the sensing signal, I-V measurements were performed with FTO without MnO_2 coating and with MnO_2 coating as a working electrode and comparatively presented in SI Figure 6b. It is observed that the analytical signal is 10 times more intense due to the presence of MnO_2. In this case, the iso-electric point (IEP) of MnO_2 (IEP = 4-5)[56] is higher than the pH value of the electrolyte solution (pH = 7.5). As a result, the surface of MnO_2 is charged negatively that enhances surface adsorption of MB molecule due to its intrinsic positive charge.

Dengue virus infections affect 390 million globally and 0.15 million in India.[57,58] There exist four different DENV serotypes that are difficult to distinguish except NAAT reactions or ELISA assays

involving costly antibodies.[59] Moreover, cross-infection with different serotypes has also been linked with severe dengue.[57] Therefore, an ultrasensitive NAAT assay that can be carried out at near ambient temperature without using real-time PCR would be invaluable towards sequence-specific detection of DENV serotypes at limited-resource settings. With this intended application, we designed a primer and complementary circular DNA where the latter was synthesized using self-annealing ligation. The primer carried a DENV serotype-2 sequence that would anneal to the complementary region in the circular DNA and trigger rolling circle amplification (RCA), an isothermal amplification reaction doable at 30°C. The redox probe MB would bind to the DNA electrostatically as well as intercalation into the DNA ladder structure (π-stacking).[24] For no-target control (NTC) samples, a large amount of free MB was available (due to the absence of any amplicon) and responsible for higher charge transfer at electrolyte/FM550 electrode interface resulting in a higher magnitude of reduced peak current. Post amplification for samples containing the primer (target control or TC samples), a larger concentration of amplicons (i.e., replicated DNA) were generated that interacts with MB and consequently decreased the effective MB in the electrolyte solution. Hence, the reduction peak current would drop significantly and enable the detection of DNA amplified samples (Figure 4a and b).

Figure 4c depicts the endpoint (i.e., after the completion) I-V response of RCA reaction products (primer concentration 20 nM, MB concentration 100 μM, LRCA reaction) averaged over $n = 5$ replicates. Both the experiments (RCA as well as electrochemical measurement) have been performed at ambient temperature. Therefore, the electrochemical RCA, if successful and sensitive enough, would be highly utilitarian in detecting DENV and its serotypes in limited-resource settings. Our EBSD test results for electrochemical end-point RCA have been in

agreement with the aforementioned explanation, where the peak current magnitude for NTC samples was ~3 times higher than that of TC samples with a change in peak current (ΔI) of 6.31 μA (Figure 4c). The EIS measurements have been performed on endpoint LRCA reaction products as shown in Figure 4d. The inset of Figure 4d shows the EEC diagram. The semicircular section in the high-frequency region corresponds to electron transfer limited process and subsequent charge transfer resistance (R_{ct}) equals the semicircular diameter. The R_{ct} -value for TC sample is observed three times higher than that of the NTC sample (SI Table 3) which implied that the "free" MB has been captured by replicated dsDNA and a very low amount is available for charge transfer. These results are in synchronization with our hypothesis.

Figure 4e presents the signal 's' for 7 different devices with TC having 20 nM primer concentration (10^{10} initial target copies). The signal 's' values obtained for all the 7-devices are found to be more than 35% which assured good sensitivity and reproducibility of the devices. The signal 's' of our device is calculated as $s = [I_0 - I_1]/I_0 \times 100\%$, where I_0 and I_1 are the magnitude of reduction peak current for NTC and TC samples, respectively. This method of quantification has also been formerly adapted in DNA amplification detection by M. Tsaloglou et al. in electrochemical detection of RPA amplified product, and by Won et al. in the detection of real-time electrochemical PCR.[13,19,60] It has also been noticed that the electrode holds consistent performance over the storage duration of at least 6 months.

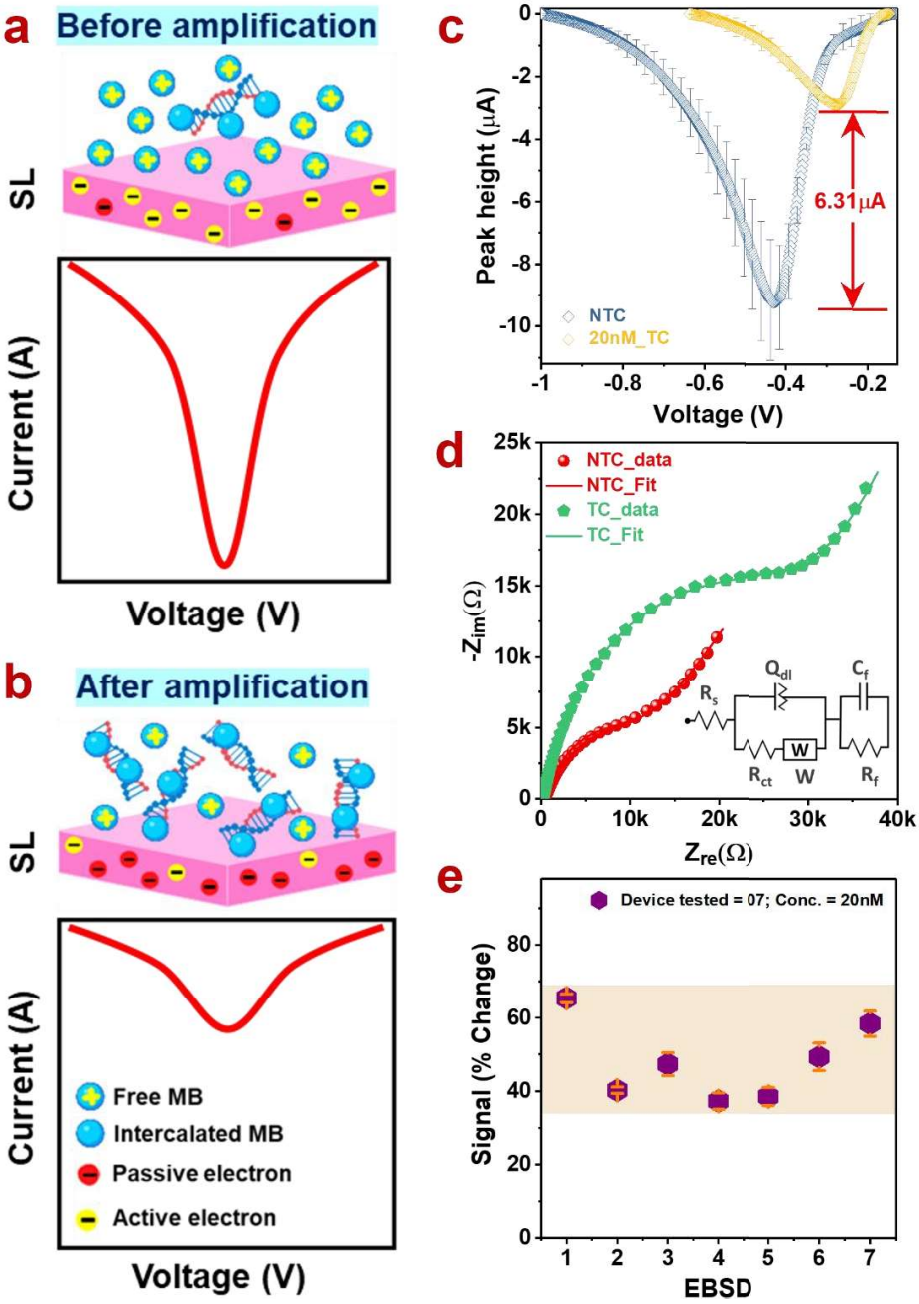

Figure 4 Electroanalytical results for NTC and TC in LRCA reaction and sensing principle. (a, b) Schematic representation of the electrochemical DNA detection approach. (c) I-V characteristics (baseline corrected) for NTC and TC in LRCA reaction (MB concentration 100 μM, primer concentration 20 nM) averaged over n=5 replicates. (d) EIS Nyquist plots for NC and PC for LRCA reaction (MB concentration 100 μM, primer concentration 20 nM; Inset shows the equivalent circuit diagram). (e) Statistical data showing % change before and after amplification for 7 different devices for LRCA reactions averaged over n=5 replicates on each device.

3.5. Limit of Detection Study for End-point Electrochemical HRCA and PCR:

The sensitivity of the EBSD using FM550 electrode was evaluated for end-point electrochemical HRCA and compared with those obtained from real-time PCR instrument-based fluorescence endpoint readout. For endpoint HRCA, the primer carrying the DENV sequence was varied between 2 fM to 20 pM with 100 μM of MB as the redox probe concentration. Percentage change in peak current is computed with respect to NTC and the signal $'s'$ for all DNA concentrations of EBSD (Figure 5a) was compared with relative end-fluorescence with respect to NTC (Figure 5b). The data presented in Figure 5a was replicated with six separate devices (EBSD 1 – 6) for each initial target (primer) concentration. Also, the peak current for target copies 0, 2 fM, 0.2 pM, and 20 pM were presented in SI Figure 7a. Approximate 40% current change has been obtained for the lowest concentration of 2 fM, while 55 – 60% change was detected for 20 fM. The results demonstrate a similar degree of change in peak current for all the devices across the tested concentrations, implying a high degree of reproducibility (Figure 5a). When compared with end-point fluorescence measurement (Figure 5b), our device showed comparable sensing ability. Conclusively, EBSD has achieved a detection limit of 2 fM (1.2 x 10^3 copies/μL) of DENV sequence DNA for end-point RCA reaction products. The analytical sensitivity of our device was similar to published electrochemical RCA platforms employing methylene blue as the redox probe used for sensing DNA methylation (LoD 1 fM, differential pulse voltammetry)[61] or for *Pseudomonas aeruginosa* 16S rRNA detection (LoD 10 fM, differential pulse voltammetry).[62]

Next, the analytical sensitivity of the device was tested for detecting the vancomycin resistance-associated regulator gene (*vraR*) gene in *S. aureus*[63]. *S. aureus* is an opportunistic pathogen that

is responsible for over 1,20,000 infections and 20,000 deaths in 2017 in the United States alone.[64] Moreover, multi-drug resistant *S. aureus* (MRSA, e.g., N315 stain used for genomic DNA isolation in this study) accounted for 25% of all *S. aureus* infections in European countries.[65] Therefore, we anticipated that a sensitive electrochemical PCR enabling the detection of *vraR* gene from the MRSA N315 strain genomic DNA would provide a valuable molecular diagnosis tool in *S. aureus* induced bacteraemia prevention. In our experiment, the electrochemical PCR conducted for detecting S. *aureus* genomic DNA on $10^1 – 10^4$ copies for *vraR* gene were compared with the change in cycle threshold values (ΔC_t) obtained from real-time PCR experiments (Figure 5c and 5d). Conventionally, C_t value in real-time PCR is defined as the cycle at which the amplification-derived fluorescence crosses a baseline threshold. We observed that our device was able to detect as low as 10^3 copies with a ~12% current change compared to NTC (Figure 5c). The analytical sensitivity of the method was comparable to published reports of electrochemical PCR nucleic acid-sensing employing methylene blue as the redox mediator such as detection of Lambda phage DNA using a microfluidic flow-through device (489 bp, LoD 2 x 10^4 copies, measurement using square wave voltammetry)[66] or *Chlamydia trachomatis* DNA templates (612 bp, LoD 10^3 copies, measurement using square wave voltammetry).[60] Overall, the limit of detection study conducted on isothermal amplification and conventional PCR indicated that the device has similar analytical sensitivity as that of the real-time fluorescence measurement.

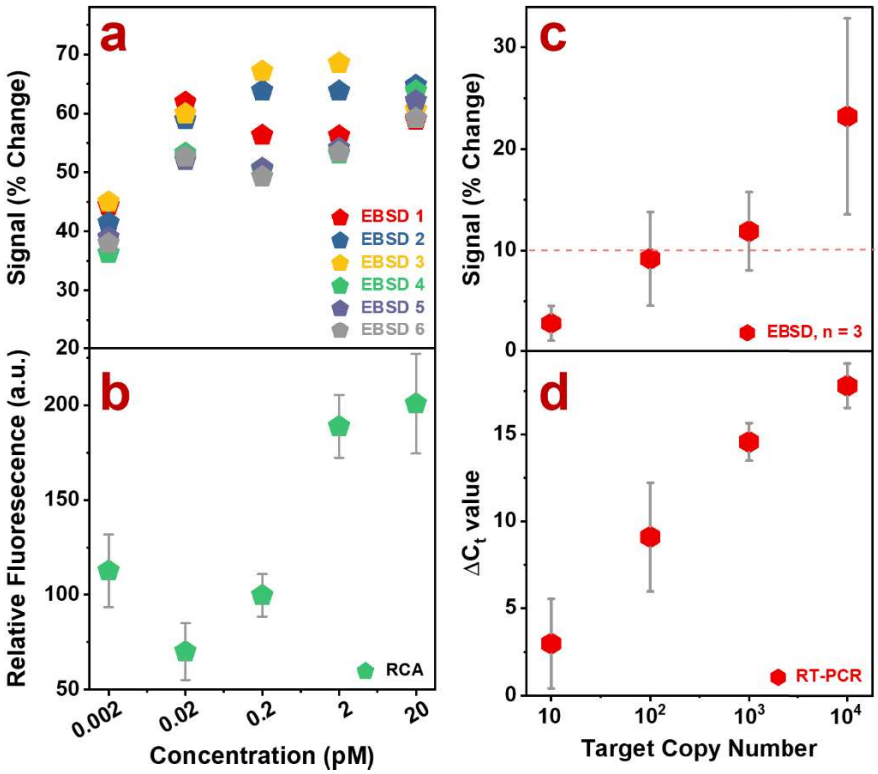

Figure 5 Limit of detection study of RCA and RT-PCR reactions comparing EBSD performance with standard detection methods. (a) Plot of signal s, the % change in the peak current for different target DNA concentrations (0.002 to 20 pM) w.r.t. NTC from the I-V measurement on FM550 electrode for RCA reaction products for n=6 EBSD. (b) Relative fluorescence of RCA reaction products w.r.t. NTC for n=5 samples. (c) Plot of signal s, the % change in the peak current for different target DNA concentrations (0.002 to 20 pM) w.r.t. NTC from the I-V measurement on FM550 electrode for RT-PCR reaction products for n=6 EBSD. (d) ΔC_t value of RT-PCR reaction products w.r.t. NTC for n=3 samples.

4. Conclusion:

Detection of pathogen nucleic acid sequences through NAAT or isothermal NAAT is of utmost importance in molecular diagnosis. However, such bioanalytical assays are typically carried out using real-time PCR which predominantly remains confined to centralized labs. Adoption of electrochemical methods of analysing NAATs, on other hand, would decentralize the assays due to the low cost of the instruments involved (i.e., a conventional thermal cycler and

electrochemical workstation). In this regard, most of the assays concerning electrochemical readout of NAATs have utilized electrodes made of novel metals that are costly and not commonly available for in-house fabrication. Any electrode materials based out of transition metal oxides would in turn be inexpensive with a wide range of tunability owing to their versatile electronic states.

The current work shows that the electronic state of MnO_2 can be successfully tailored by creating O_2 vacancies through annealing at various elevated temperatures. This principle was utilized in fabricating an affordable, speedy, and user-friendly DNA amplicon detection device. This device utilizes bi-electrode geometry to read out a change in current signals resulted from the interaction of DNA with cationic dye MB in amplified samples. Finally, the electrodes were utilized in detecting dengue virus DNA sequence (using electrochemical RCA conducted at 30°C) and *S. aureus* genomic DNA (using electrochemical PCR). Along with 4 – 5 orders of dynamic range, the analytical sensitivity of the device was in the order of 10^3 copies/μL for RCA and 10^3 copies for PCR and was comparable to real-time fluorescence measurement assays carried out in RT-PCR instruments.

Supplementary Information:

Redox couple for Methylene blue (MB), Schematic for spin coating deposition method, Picture of the fabricated electrochemical bi-electrode sensing device (EBSD), UV-Visible spectroscopy results, Equivalent circuit diagram for AC conductivity measurements, Electroanalytical results of FM550 device, Peak current curves of limit of detection study for (a) RCA reaction. (b) RT-PCR reaction.

Acknowledgement:

This work was supported by the Bennett University Ph.D. fellowship to Tanvi Agarkar, Bennett University Seed Grant funding, and Early Career Research Grant (No. ECR/20l8/001399) awarded by the Department of Science and Technology Science and Engineering Research Board, India.

References:

[1] P.T. Monis, S. Giglio, Nucleic acid amplification-based techniques for pathogen detection and identification, Infect. Genet. Evol. 6 (2006) 2–12. https://doi.org/10.1016/j.meegid.2005.08.004.

[2] L. Garibyan, N. Avashia, Polymerase chain reaction, J. Invest. Dermatol. 133 (2013) 1–4. https://doi.org/10.1038/jid.2013.1.

[3] C.T. Wittwer, M.G. Herrmann, Rapid thermal cycling and PCR kinetics, in: PCR Appl. Protoc. Funct. Genomics, Academic Press, 1999: pp. 211–229. https://doi.org/10.1016/b978-012372185-3/50015-8.

[4] L.M. Zanoli, G. Spoto, Isothermal amplification methods for the detection of nucleic acids in microfluidic devices, Biosensors. 3 (2013) 18–43. https://doi.org/10.3390/bios3010018.

[5] E. Navarro, G. Serrano-Heras, M.J. Castaño, J. Solera, Real-time PCR detection chemistry, Clin. Chim. Acta. 439 (2015) 231–250. https://doi.org/10.1016/j.cca.2014.10.017.

[6] M.N. Krosch, A. McNevin, J. Cook, C. Allen, D. Keatinge, Fluorescent dye-based detection of trace DNA on forensic tapelifts from worn shirts, Aust. J. Forensic Sci. 00 (2020) 1–12.

https://doi.org/10.1080/00450618.2019.1711177.

[7] S. Chavda, Y. Liu, B. Babu, R. Davis, A. Sielaff, J. Ruprich, L. Westrate, C. Tronrud, A. Ferguson, A. Franks, S. Tzou, C. Adkins, T. Rice, H. MacKay, J. Kluza, S.A. Tahir, S. Lin, K. Kiakos, C.D. Bruce, W.D. Wilson, J.A. Hartley, M. Lee, Hx, a novel fluorescent, minor groove and sequence specific recognition element: Design, synthesis, and DNA binding properties of p - anisylbenzimidazole-imidazole/pyrrole-containing polyamides, Biochemistry. 50 (2011) 3127–3136. https://doi.org/10.1021/bi102028a.

[8] A.I. Dragan, R. Pavlovic, J.B. McGivney, J.R. Casas-Finet, E.S. Bishop, R.J. Strouse, M.A. Schenerman, C.D. Geddes, SYBR Green I: Fluorescence properties and interaction with DNA, J. Fluoresc. 22 (2012) 1189–1199. https://doi.org/10.1007/s10895-012-1059-8.

[9] J.A. Sikorsky, D.A. Primerano, T.W. Fenger, J. Denvir, DNA damage reduces Taq DNA polymerase fidelity and PCR amplification efficiency, Biochem. Biophys. Res. Commun. 355 (2007) 431–437. https://doi.org/10.1016/j.bbrc.2007.01.169.

[10] M. Nilsson, M. Gullberg, F. Dahl, K. Szuhai, A.K. Raap, Real-time monitoring of rolling-circle amplification using a modified molecular beacon design., Nucleic Acids Res. 30 (2002) 1–7. https://doi.org/10.1093/nar/gnf065.

[11] A. V. Hadjinicolaou, V.L. Demetriou, M.A. Emmanuel, C.K. Kakoyiannis, L.G. Kostrikis, Molecular beacon-based real-time PCR detection of primary isolates of salmonella typhimurium and salmonella enteritidis in environmental and clinical samples, BMC Microbiol. 9 (2009) 1–14. https://doi.org/10.1186/1471-2180-9-97.

[12] E. Paleček, M. Bartošík, Electrochemistry of nucleic acids, Chem. Rev. 112 (2012) 3427–3481. https://doi.org/10.1021/cr200303p.

[13] M.N. Tsaloglou, A. Nemiroski, G. Camci-Unal, D.C. Christodouleas, L.P. Murray, J.T. Connelly, G.M. Whitesides, Handheld isothermal amplification and electrochemical detection of DNA in resource-limited settings, Anal. Biochem. 543 (2018) 116–121. https://doi.org/10.1016/j.ab.2017.11.025.

[14] J. Movilli, R.W. Kolkman, A. Rozzi, R. Corradini, L.I. Segerink, J. Huskens, Increasing the Sensitivity of Electrochemical DNA Detection by a Micropillar-Structured Biosensing Surface, Langmuir. 36 (2020) 4272–4279. https://doi.org/10.1021/acs.langmuir.0c00144.

[15] H.F. Cui, T. Bin Xu, Y.L. Sun, A.W. Zhou, Y.H. Cui, W. Liu, J.H.T. Luong, Hairpin DNA as a biobarcode modified on gold nanoparticles for electrochemical DNA detection, Anal. Chem. 87 (2015) 1358–1365. https://doi.org/10.1021/ac504206n.

[16] R. Rosario, R. Mutharasan, Nucleic acid electrochemical and electromechanical biosensors: A review of techniques and developments, Rev. Anal. Chem. 33 (2014) 213–230. https://doi.org/10.1515/revac-2014-0017.

[17] N. Nagatani, K. Yamanaka, M. Saito, R. Koketsu, T. Sasaki, K. Ikuta, T. Miyahara, E. Tamiya, Semi-real time electrochemical monitoring for influenza virus RNA by reverse transcription loop-mediated isothermal amplification using a USB powered portable potentiostat, Analyst. 136 (2011) 5143–5150. https://doi.org/10.1039/c1an15638a.

[18] K. Hsieh, A.S. Patterson, B.S. Ferguson, K.W. Plaxco, H.T. Soh, Rapid, sensitive, and

quantitative detection of pathogenic DNA at the point of care through microfluidic electrochemical quantitative loop-mediated isothermal amplification, Angew. Chemie - Int. Ed. 51 (2012) 4896–4900. https://doi.org/10.1002/anie.201109115.

[19] M.U. Ahmed, S. Nahar, M. Safavieh, M. Zourob, Real-time electrochemical detection of pathogen DNA using electrostatic interaction of a redox probe, Analyst. 138 (2013) 907–915. https://doi.org/10.1039/c2an36153a.

[20] J. Zhang, S. Song, L. Zhang, L. Wang, H. Wu, D. Pan, C. Fan, Sequence-specific detection of femtomolar DNA via a chronocoulometric DNA sensor (CDS): Effects of nanoparticle-mediated amplification and nanoscale control of DNA assembly at electrodes, J. Am. Chem. Soc. 128 (2006) 8575–8580. https://doi.org/10.1021/ja061521a.

[21] J. Zhang, S. Song, L. Wang, D. Pan, C. Fan, A gold nanoparticle-based chronocoulometric dna sensor for amplified detection of dna, Nat. Protoc. 2 (2007) 2888–2895. https://doi.org/10.1038/nprot.2007.419.

[22] B. Meric, K. Kerman, D. Ozkan, P. Kara, S. Erensoy, U.S. Akarca, M. Mascini, M. Ozsoz, Electrochemical DNA biosensor for the detection of TT and hepatitis B virus from PCR amplified real samples by using, Talanta. 56 (2002) 837–846. https://doi.org/10.1016/S0039-9140(01)00650-6.

[23] M.A. Hasnat, J.A. Safwan, M.S. Islam, Z. Rahman, M.R. Karim, T.J. Pirzada, A.J. Samed, M.M. Rahman, Electrochemical decolorization of Methylene blue at Pt electrode in KCl solution for environmental remediation, J. Ind. Eng. Chem. 21 (2015) 787–791.

https://doi.org/10.1016/j.jiec.2014.04.013.

[24] E.M. Boon, N.M. Jackson, M.D. Wightman, S.O. Kelley, M.G. Hill, J.K. Barton, Intercalative stacking: A critical feature of DNA charge-transport electrochemistry, J. Phys. Chem. B. 107 (2003) 11805–11812. https://doi.org/10.1021/jp030753i.

[25] P.A. Rasheed, N. Sandhyarani, Electrochemical DNA sensors based on the use of gold nanoparticles: a review on recent developments, Microchim. Acta. 184 (2017) 981–1000. https://doi.org/10.1007/s00604-017-2143-1.

[26] K. Yamanaka, M.C. Vestergaard, E. Tamiya, Printable electrochemical biosensors: A focus on screen-printed electrodes and their application, Sensors (Switzerland). 16 (2016) 1–16. https://doi.org/10.3390/s16101761.

[27] M.M. Rahman, S.B. Khan, G. Gruner, M.S. Al-Ghamdi, M.A. Daous, A.M. Asiri, Chloride ion sensors based on low-dimensional α-MnO 2-Co3O4 nanoparticles fabricated glassy carbon electrodes by simple I-V technique, Electrochim. Acta. 103 (2013) 143–150. https://doi.org/10.1016/j.electacta.2013.04.067.

[28] Z.L. Wu, C.K. Li, J.G. Yu, X.Q. Chen, MnO2/reduced graphene oxide nanoribbons: Facile hydrothermal preparation and their application in amperometric detection of hydrogen peroxide, Sensors Actuators, B Chem. 239 (2017) 544–552. https://doi.org/10.1016/j.snb.2016.08.062.

[29] D. Rao, X. Zhang, Q. Sheng, J. Zheng, Highly improved sensing of dopamine by using glassy carbon electrode modified with MnO2, graphene oxide, carbon nanotubes and gold

nanoparticles, Microchim. Acta. 183 (2016) 2597–2604. https://doi.org/10.1007/s00604-016-1902-8.

[30] M. Huang, X.L. Zhao, F. Li, L.L. Zhang, Y.X. Zhang, Facile synthesis of ultrathin manganese dioxide nanosheets arrays on nickel foam as advanced binder-free supercapacitor electrodes, J. Power Sources. 277 (2015) 36–43. https://doi.org/10.1016/j.jpowsour.2014.12.005.

[31] D. Su, H.J. Ahn, G. Wang, Hydrothermal synthesis of α-MnO2 and β-MnO 2 nanorods as high capacity cathode materials for sodium ion batteries, J. Mater. Chem. A. 1 (2013) 4845–4850. https://doi.org/10.1039/c3ta00031a.

[32] S. Yang, G. Li, G. Wang, J. Zhao, X. Gao, L. Qu, Synthesis of Mn3O4 nanoparticles/nitrogen-doped graphene hybrid composite for nonenzymatic glucose sensor, Sensors Actuators, B Chem. 221 (2015) 172–178. https://doi.org/10.1016/j.snb.2015.06.110.

[33] Y.T. Tsai, T.C. Chang, C.C. Lin, L.S. Chiang, S.C. Chen, S.M. Sze, T.Y. Tseng, Effect of top electrode material on resistive switching characteristics in MnO 2 nonvolatile memory devices, ECS Trans. 41 (2011) 475–482. https://doi.org/10.1149/1.3633064.

[34] M.K. Yang, J.W. Park, T.K. Ko, J.K. Lee, Bipolar resistive switching behavior in Ti/ MnO2 /Pt structure for nonvolatile memory devices, Appl. Phys. Lett. 95 (2009) 95–98. https://doi.org/10.1063/1.3191674.

[35] S. Pishdadian, A.M. Shariati Ghaleno, Influences of annealing temperature on the optical and structural properties of manganese oxide thin film by Zn doping from sol-gel technique,

Acta Phys. Pol. A. 123 (2013) 741–745. https://doi.org/10.12693/APhysPolA.123.741.

[36] X. Huang, X. Gao, Q. Xue, C. Wang, R. Zhang, Y. Gao, Z. Han, Impact of oxygen vacancies on TiO2 charge carrier transfer for photoelectrochemical water splitting, Dalt. Trans. 49 (2020) 2184–2189. https://doi.org/10.1039/c9dt04374h.

[37] S. Wißmann, K.D. Becker, Localization of electrons in nonstoichiometric SrFeO3-Δ, Solid State Ionics. 85 (1996) 279–283. https://doi.org/10.1016/0167-2738(96)00071-9.

[38] S.A. Ansari, M.M. Khan, S. Kalathil, A. Nisar, J. Lee, M.H. Cho, Oxygen vacancy induced band gap narrowing of ZnO nanostructures by an electrochemically active biofilm, Nanoscale. 5 (2013) 9238–9246. https://doi.org/10.1039/c3nr02678g.

[39] S. Chen, Y. Xiao, Y. Wang, Z. Hu, H. Zhao, W. Xie, A facile approach to prepare black TiO2 with oxygen vacancy for enhancing photocatalytic activity, Nanomaterials. 8 (2018) 1–16. https://doi.org/10.3390/nano8040245.

[40] S.R. Ede, A. Ramadoss, S. Anantharaj, U. Nithiyanantham, S. Kundu, Enhanced catalytic and supercapacitor activities of DNA encapsulated β-MnO2 nanomaterials, Phys. Chem. Chem. Phys. 16 (2014) 21846–21859. https://doi.org/10.1039/c4cp02884h.

[41] J.S. Sherin, M. Haris, D.S. Manoj, J. Koshy, J.K. Thomas, Enhanced electrochemical properties in nanostructured β-MnO2, synthesized through a single step auto-igniting modified combustion technique., Int. J. ChemTech Res. 10 (2017) 647–655.

[42] M.M. El-Nahass, H.S. Soliman, A. El-Denglawey, Absorption edge shift, optical conductivity,

and energy loss function of nano thermal-evaporated N-type anatase TiO2 films, Appl. Phys. A Mater. Sci. Process. 122 (2016) 1–10. https://doi.org/10.1007/s00339-016-0302-6.

[43] B.I. Supanan Anuchai, Sukon Phanichphant, Doldet Tantraviwat, Prayoonsak Pluengphon, Thiti Bovornratanaraks, Low temperature preparation of oxygen-deficient tin dioxide nanocrystals and a role of oxygen vacancy in photocatalytic activity improvement, J. Colloid Interface Sci. (2018) 105–114.

[44] G. Couturier, J. Salardenne, C. Sribi, M. Rosso, Electronic and ionic conductivity measurements in ionic conductors with a high band gap, Solid State Ionics. 9–10 (1983) 699–705. https://doi.org/10.1016/0167-2738(83)90317-X.

[45] D.S. Shang, L. Shi, J.R. Sun, B.G. Shen, F. Zhuge, R.W. Li, Y.G. Zhao, Improvement of reproducible resistance switching in polycrystalline tungsten oxide films by in situ oxygen annealing, Appl. Phys. Lett. 96 (2010) 21–24. https://doi.org/10.1063/1.3300637.

[46] W. Li, R. Zeng, Z. Sun, D. Tian, S. Dou, Uncoupled surface spin induced exchange bias in α-MnO 2 nanowires, Sci. Rep. 4 (2014). https://doi.org/10.1038/srep06641.

[47] R.A. Davoglio, G. Cabello, J.F. Marco, S.R. Biaggio, Synthesis and characterization of α-MnO2 nanoneedles for electrochemical supercapacitors, Electrochim. Acta. 261 (2018) 428–435. https://doi.org/10.1016/j.electacta.2017.12.118.

[48] X. Zhao, X. Liu, F. Li, M. Huang, MnO2@NiO nanosheets@nanowires hierarchical structures with enhanced supercapacitive properties, J. Mater. Sci. 55 (2020) 2482–2491. https://doi.org/10.1007/s10853-019-04112-4.

[49] Y. Yang, J. Huang, S. Wang, S. Deng, B. Wang, G. Yu, Catalytic removal of gaseous unintentional POPs on manganese oxide octahedral molecular sieves, Appl. Catal. B Environ. 142–143 (2013) 568–578. https://doi.org/10.1016/j.apcatb.2013.05.048.

[50] G. Zhu, J. Zhu, W. Jiang, Z. Zhang, J. Wang, Y. Zhu, Q. Zhang, Surface oxygen vacancy induced A-MnO2nanofiber for highly efficient ozone elimination, Appl. Catal. B Environ. 209 (2017) 729–737. https://doi.org/10.1016/j.apcatb.2017.02.068.

[51] S.E. Chun, S. Il Pyun, G.J. Lee, A study on mechanism of charging/discharging at amorphous manganese oxide electrode in 0.1 M Na2SO4 solution, Electrochim. Acta. 51 (2006) 6479–6486. https://doi.org/10.1016/j.electacta.2006.04.034.

[52] Q. Xie, C. Xiang, Y. Yuan, Y. Zhang, L. Nie, S. Yao, A novel dual-impedance-analysis EQCM system - Investigation of bovine serum albumin adsorption on gold and platinum electrode surfaces, J. Colloid Interface Sci. 262 (2003) 107–115. https://doi.org/10.1016/S0021-9797(03)00196-6.

[53] M.A. Macdonald, H.A. Andreas, Method for equivalent circuit determination for electrochemical impedance spectroscopy data of protein adsorption on solid surfaces, Electrochim. Acta. 129 (2014) 290–299. https://doi.org/10.1016/j.electacta.2014.02.046.

[54] C. He, Z. Liu, H. Peng, Y. Yang, D. Shi, X. Xie, Room-temperature catalytic growth of hierarchical urchin-like MnO2 spheres on graphene to achieve silver-doped nanocomposites with improved supercapacitor performance, Electrochim. Acta. 222 (2016) 1393–1401. https://doi.org/10.1016/j.electacta.2016.11.116.

[55] C. Li, H. Yamahara, Y. Lee, H. Tabata, J.J. Delaunay, CuO nanowire/microflower/nanowire modified Cu electrode with enhanced electrochemical performance for non-enzymatic glucose sensing, Nanotechnology. 26 (2015) 305503. https://doi.org/10.1088/0957-4484/26/30/305503.

[56] P.R. Solanki, A. Kaushik, V. V. Agrawal, B.D. Malhotra, Nanostructured metal oxide-based biosensors, NPG Asia Mater. 3 (2011) 17–24. https://doi.org/10.1038/asiamat.2010.137.

[57] K.M. Soo, B. Khalid, S.M. Ching, H.Y. Chee, Meta-analysis of dengue severity during infection by different dengue virus serotypes in primary and secondary infections, PLoS One. 11 (2016) 4–14. https://doi.org/10.1371/journal.pone.0154760.

[58] DENGUE/DHF SITUATION IN INDIA :: National Vector Borne Disease Control Programme (NVBDCP), (n.d.). https://nvbdcp.gov.in/index4.php?lang=1&level=0&linkid=431&lid=3715 (accessed August 19, 2021).

[59] I. Bosch, A. Reddy, H. de Puig, J.E. Ludert, F. Perdomo-Celis, C.F. Narváez, A. Versiani, D. Fandos, M.L. Nogueira, M. Singla, R. Lodha, G.R. Medigeshi, I. Lorenzana, H.V. Ralde, M. Gélvez-Ramírez, L.A. Villar, M. Hiley, L. Mendoza, N. Salcedo, B.B. Herrera, L. Gehrke, Serotype-specific detection of dengue viruses in a nonstructural protein 1-based enzyme-linked immunosorbent assay validated with a multi-national cohort, PLoS Negl. Trop. Dis. 14 (2020) 1–15. https://doi.org/10.1371/journal.pntd.0008203.

[60] B.Y. Won, S. Shin, S. Baek, Y.L. Jung, T. Li, S.C. Shin, D.Y. Cho, S.B. Lee, H.G. Park, Investigation of the signaling mechanism and verification of the performance of an

electrochemical real-time PCR system based on the interaction of methylene blue with DNA, Analyst. 136 (2011) 1573–1579. https://doi.org/10.1039/c0an00695e.

[61] H. Liu, J. Luo, L. Fang, H. Huang, J. Deng, J. Huang, S. Zhang, Y. Li, J. Zheng, An electrochemical strategy with tetrahedron rolling circle amplification for ultrasensitive detection of DNA methylation, Biosens. Bioelectron. 121 (2018) 47–53. https://doi.org/10.1016/j.bios.2018.07.055.

[62] H. Zhou, S. Duan, J. Huang, F. He, An ultrasensitive electrochemical biosensor forPseudomonas aeruginosaassay based on a rolling circle amplification-assisted multipedal DNA walker, Chem. Commun. 56 (2020) 6273–6276. https://doi.org/10.1039/d0cc01619e.

[63] S. Boyle-Vavra, S. Yin, R.S. Daum, The VraS/VraR two-component regulatory system required for oxacillin resistance in community-acquired methicillin-resistant Staphylococcus aureus, FEMS Microbiol. Lett. 262 (2006) 163–171. https://doi.org/10.1111/j.1574-6968.2006.00384.x.

[64] A.P. Kourtis, K. Hatfield, J. Baggs, Y. Mu, I. See, E. Epson, J. Nadle, M.A. Kainer, G. Dumyati, S. Petit, S.M. Ray, D. Ham, C. Capers, H. Ewing, N. Coffin, L.C. McDonald, J. Jernigan, D. Cardo, Vital Signs: Epidemiology and Recent Trends in Methicillin-Resistant and in Methicillin-Susceptible Staphylococcus aureus Bloodstream Infections — United States , MMWR. Morb. Mortal. Wkly. Rep. 68 (2019) 214–219. https://doi.org/10.15585/mmwr.mm6809e1.

[65] European Centre for Disease Prevention and Control (ECDC), European Centre for Disease

Prevention and Control. Antimicrobial resistance surveillance in Europe 2014. Annual Report of the European Antimicrobial Resistance Surveillance Network (EARS-Net). Stockholm: ECDC; 2015, 2015. https://doi.org/10.2900/23549.

[66] T.H. Fang, N. Ramalingam, D. Xian-Dui, T.S. Ngin, Z. Xianting, A.T. Lai Kuan, E.Y. Peng Huat, G. Hai-Qing, Real-time PCR microfluidic devices with concurrent electrochemical detection, Biosens. Bioelectron. 24 (2009) 2131–2136. https://doi.org/10.1016/j.bios.2008.11.009.